Journal Pre-proof

Atmospheric dynamics in high obliquity planets

A.H. Lobo, S. Bordoni

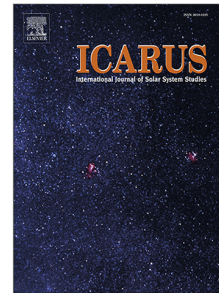Please cite this article as: A.H. Lobo and S. Bordoni, Atmospheric dynamics in high obliquity planets. *Icarus* (2019), doi: https://doi.org/10.1016/j.icarus.2019.113592.

This is a PDF file of an article that has undergone enhancements after acceptance, such as the addition of a cover page and metadata, and formatting for readability, but it is not yet the definitive version of record. This version will undergo additional copyediting, typesetting and review before it is published in its final form, but we are providing this version to give early visibility of the article. Please note that, during the production process, errors may be discovered which could affect the content, and all legal disclaimers that apply to the journal pertain.

Atmospheric Dynamics in High Obliquity Planets

Lobo, A. H. & Bordoni, S.

California Institute of Technology

Abstract

Ongoing discoveries of terrestrial exoplanets and the desire to determine their habitability have created an increasing demand for studies of a wide range of climatic regimes and atmospheric circulations. These studies have, in turn, challenged our understanding of our own planet's atmospheric dynamics and provided new frameworks with which we can further our understanding of planetary atmospheres. In this work, we use an idealized moist general circulation model in aquaplanet configuration to study the atmospheric circulation of terrestrial planets with high obliquities. With seasonally varying insolation forcing and a shallow slab ocean as a lower boundary, we emphasize seasonal phenomena that might not be captured in simulations with annual-mean forcing and that might involve nonlinear behaviors. By progressively increasing obliquity, we explore the response of the large-scale atmospheric circulation to more extreme seasonal cycles and a reversed annual-mean equator-to-pole insolation distribution, and its impact on the energy and water cycles. We show that for high obliquities, the large-scale atmospheric circulation and the meridional energy transport are dominated by seasonally reversing broad cross-equatorial Hadley cells that transport energy from the summer to the winter hemisphere and significantly mitigate temperature extremes. These overturning cells also play a major role in shaping the planet's hydrological cycle, with the associated ascending branches and precipitation convergence zones becoming progressively broader and more poleward shifted into the summer hemisphere with higher obliquities. While not embedded within the Hadley cell ascending branches, the hot summer poles of high obliquity planets experience nonnegligible precipita-

tion during and at the end of the warm season: during the summer, lower-level moist static energy maxima at the summer poles force locally enhanced convective activity. As temperatures rapidly drop at the end of the summer and convective activity decreases, the water-holding capacity of the atmosphere decreases and water vapor stored in the atmospheric column rapidly condenses out, extending the duration of the summer pole rainy season into the corresponding autumn. Our study reveals novel understanding of how atmospheric dynamics might influence a planet's overall climate and its variability.

Keywords: Planetary Atmospheres, High Obliquity, Habitability

1. Introduction

The recent surge in exoplanet discoveries and the promise of improved detection limits in the near future have inspired a new wave of research in planetary climate. It is now necessary to consider a much larger range of possible orbital

5   parameters, and surface and atmospheric conditions than what was previously seen in studies of our solar system's rocky planets. Yet, this must be done while working with a drastically smaller dataset for each planet. Models of different complexity have hence provided a fundamental tool to further our understanding of atmospheric behavior of these planets under a wide range of

10   physical and dynamical regimes. These include studies such as Del Genio & Zhou (1996), Merlis & Schneider (2010), Faulk et al. (2017) and many others summarized in the review paper by Showman et al. (2013). Idealized models have proven particularly useful because they allow for investigations of the fundamental mechanisms controlling climate without requiring specific knowledge

15   about the atmospheric composition and chemistry.

Earth is, of course, the most extensively studied terrestrial planet and we would benefit from extrapolating what we know about our planet to those newly discovered. However, we still struggle to disentangle the impact of dynamical, thermodynamic and boundary layer processes on Earth's large-scale atmo-

20   spheric circulation. For example, predicting how the Hadley cell responds, in

terms of its strength and extent, to changes in radiative forcing and planetary parameters is still an active area of research, despite being a first order problem for characterizing the large-scale circulation of an Earth-like planet (e.g. Faulk et al., 2017; Singh, 2019; Guendelman & Kaspi, 2018). Hence, we are faced

25 with the opportunity and the need to advance two fields concurrently. By testing competing atmospheric theories over a broader range of parameters we can both improve our understanding of the processes we encounter on Earth and better characterize different atmospheric regimes we might encounter in terrestrial planets. This is the approach taken by many of the previously mentioned

30 papers over a broad range of parameters. Our goal is to expand on the existing body of literature through an in depth study of the atmospheric response to varying obliquity. We focus on the seasonal response of atmospheric large-scale circulations and their relationship to the hydrological cycle.

While in fact many have explored the atmospheric circulation and associ-
35 ated climate arising in response to annual-mean solar forcing – a useful starting point – the removal of seasonal cycles prevents consideration of seasonal phenomena that are of primary importance for a planet's climate and whose dynamics remain relatively poorly understood. These include the monsoons on Earth (Schneider & Bordoni, 2008), polar clouds on Titan (Turtle et al.,
40 2009), and dust storms on Mars (Wang & Richardson, 2015). Depending on the planet's orbital parameters, seasonal cycles could be even more extreme than those we currently see on the "Earth-like" terrestrial planets in our solar system, potentially introducing nonlinearities not captured under annual-mean forcing.

In the context of seasonal cycles, exploring the impact of obliquity takes a
45 primary relevance. While Earth's obliquity has only small variations around its present-day value of 23.5°, planets within our own solar system feature much higher obliquities: Uranus has an obliquity of 97°, which places its axis of rotation nearly on the orbital plane. Other interesting cases include Pluto at 120° and Mar's past obliquity. Mars's current obliquity of 25° is very similar to
50 Earth's, but it is believed to have varied chaotically between 0 and 60° throughout its history (Laskar & Robutel, 1993; Touma & Wisdom, 1993). Interestingly,

as obliquity increases beyond 54°, a planet receives more energy at the poles than at the equator on the annual average, opposite to what is seen on planets with smaller obliquities, such as Earth. Also, high obliquity planets have very

₅₅ extreme seasonal cycles, which raises the question of how the atmospheric circulation might mitigate these variations and to what extent it could render such planets habitable. Thus, understanding how obliquity influences the climate of a planet is not only a useful theoretical exercise, but is also relevant to ongoing efforts to understand Martial paleoclimate and better characterize the climate

₆₀ of other planets in our own solar system.

To address these questions, in this paper we conduct experiments with an idealized atmospheric general circulation model in aquaplanet configuration to explore how obliquity affects the climate of an Earth-like planet. Obliquity is varied over a broad range of values, namely from 10° to 85°. The model

₆₅ makes use of a slab ocean, rather than a fully interactive ocean, which does not allow for consideration of the role of ocean dynamics in the simulated climate. There is no doubt that an ocean would have a significant impact on climates of high obliquity planets, if one existed. The ocean heat uptake, through seasonal storage and transport by oceanic currents, would prevent more extreme seasonal

₇₀ temperature changes, serving as a heat source during winter and sink during summer (Ferreira et al., 2014). In its absence, it is left to atmospheric motions to possibly mitigate imbalances implied by the solar insolation. We are interested in exploring these atmospheric features and their dynamics in these extreme climates.

₇₅ The paper is organized as follows: Section 2 introduces the general circulation model used and the numerical experiments conducted in this study. Section 3 focuses on surface climate, including surface temperatures and their relation to atmospheric energy transport. Section 4 describes the global overturning circulation, while Section 5 explores mechanisms behind the modeled

₈₀ hydrological cycle. Discussion and Conclusions follow in Section 6 and 7.

2. Methods

We utilize a 3D idealized primitive equation General Circulation Model (GCM) of an ideal-gas atmosphere, built on the Flexible Modeling System (FMS) developed by the Geophysical Fluid Dynamics Laboratory (GFDL) (Frier-
85 son et al., 2007; O'Gorman & Schneider, 2008). It is idealized in terms of the represented physics and in terms of the lower boundary, which is a completely uniform slab ocean of constant depth (aquaplanet).

The GCM is a moist model, in that it contains idealized representation of the effect of latent heat release of condensing water vapor on the dynamics through
90 a grid-scale condensation scheme and a quasi-equilibrium convection scheme (Frierson et al., 2007; O'Gorman & Schneider, 2008). The set-up is similar to that in Bordoni & Schneider (2008), with T42 horizontal resolution and 30 levels in the vertical. While somewhat coarse, the horizontal resolution is more than adequate to resolve the large-scale circulation features, such as the Hadley cell
95 and baroclinic eddies, we are interested in. Radiation is represented through a two-stream gray radiation scheme with prescribed longwave optical depth. In this study, the optical depth is only a function of pressure, comprising a well mixed CO_2-like absorber and a bottom-heavy "water vapor" absorber:

$$\tau(p) = \tau_o \left[f\left(\frac{p}{p_0}\right) + (1-f)\left(\frac{p}{p_0}\right)^4 \right] \tag{1}$$

where $\tau_o = 4.57$ and $f = 0.2$. Note that keeping τ fixed and independent of water
100 vapor concentration precludes any water vapor feedback. We also run a variant of the control set-up, in which τ depends on the local water vapor concentration (thus providing a simple representation of the water vapor feedback, Merlis & Schneider, 2010). These will hereby be referred to as the $\tau_{control}$ and τ_{wv} experiments.

105 We run the model in aquaplanet configuration, where the lower boundary is entirely covered with water (a slab ocean with constant depth). The sea surface temperature evolves according to a surface energy budget, which includes radiative fluxes and turbulent surface fluxes of latent and sensible heat. We

5

only conduct experiments with a mixed layer depth of 1 m, which is equivalent

110 to a surface heat capacity of $C_s = 4.13 \times 10^6$ J/m^2/K. Following Cronin & Emanuel (2013), a simple thermal inertia timescale for this lower boundary can be computed as $\tau = C/\lambda$, where λ is a feedback parameter given by a linearized coefficient of combined sensible, latent and longwave heat flux (c.f. Barsugli & Battisti, 1998). For $\lambda = 40$ W m^{-2} K^{-1}, as typical for the tropics (Gill, 1982), a

115 1 m ocean mixed layer depth has a thermal inertia timescale of $\sim$1 day. While the shallow mixed layer depth used here is not representative of ocean-covered surfaces on Earth (with typical ocean mixed layer depths of 50 m, which would imply an interial timescale of 2 months) and results in more extreme seasonal variations than what is seen in the annual mean (e.g., Bordoni & Schneider,

120 2008; Merlis et al., 2013; Faulk et al., 2017), it helps exaggerate the response of the seasonal cycle to obliquity changes and, hence, isolate mechanisms behind these changes.

The model is forced with a seasonal cycle of insolation of 360 days, with all other orbital parameters kept at Earth's values (see Table 1) and obliquity

125 varied systematically with values of 10, 23.5, 40, 54, 70 and 85°. All simulations are spun up from an isothermal state at rest and run for 20 years. Results are averaged over the last 15 simulated years. All statistics (including eddy fluxes) are computed from 6-hourly outputs and averaged at pentad (5 day) temporal resolution. While parameters of interest for all simulations are shown

130 in selected figures, most of the following discussion will provide an in-depth comparison between the Earth-like 23.5° and the 85° obliquity end case.

3. Surface Climate

Changes in obliquity result in a spatial and seasonal redistribution of short-wave radiation reaching the surface: while the globally and annually averaged

135 energy remains the same, as obliquity increases, the higher latitudes receive more insolation both during the summer solstice seasons and in the annual mean (Fig. 1). For Earth's obliquity (23.5°), the insolation is maximum at the equator

6

Parameter	Control Value
Radius	6371 km
Rotation Rate	7.292×10^{-5} s^{-1}
Gravity	9.80 m/s^2
Eccentricity	0
Solar Constant	1360 W/m^2
Mixed Layer Depth	1 m
Specific Heat Capacity of Lower Boundary	$\sim$ 3989.245 J/kg/K
τ_o for $\tau_{control}$	4.57
τ_o for τ_{wv}	1.39
Ref. Moisture Profile	70%
Convective Relaxation Time Scale	7200.0 s
Latent Heat of Vaporization (L_v)	2.5×10^6 J/kg
Specific Heat Capacity (c_p) of Air at Constant Pressure	1004.64 J/kg/K

Table 1: Summary of key model parameters used in all simulations.

(335 W/m^2) and decreases to 42% of this value at the poles (140 W/m^2). As obliquity is increased, the pole-to-equator insolation gradient is progressively

140 reduced, is almost flat at 54° and reverses for higher obliquity values. For the highest obliquity we consider here, on the annual average, the equator receives 226 W/m^2, which is about 63% of the values at the poles.

Over the seasonal cycle, obliquities equal to or larger than 23.5° show insolation distributions with similar behavior (Fig. 2), with the summer poles being

145 the loci of maximum insolation at solstice. The insolation contrast between the summer and winter hemispheres, however, sharply increases with increasing obliquity. For the highest obliquity value considered in this study (85°), at sum-
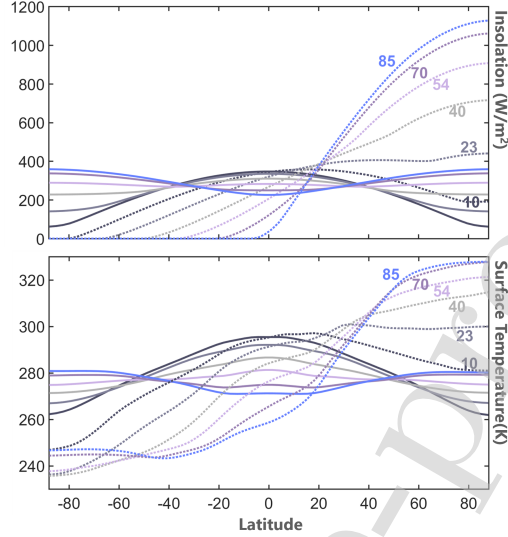
7

Figure 1: Meridional distribution of zonally averaged insolation (W/m², top) and near-surface (lowest model level) temperature (K, bottom) for $\tau_{control}$ simulations with all obliquity values. Solid lines represent annual-mean values, and dashed lines represent NH summer solstice values (at pentad 18).

mer solstice the summer pole receives upwards of 1000 W/m² and more than twice as much as the Earth-like case of 23.5°. Meanwhile, the polar night in the winter hemisphere for 85° obliquity encases the entire hemisphere and leaves even the low latitudes of the summer hemisphere in relative darkness (with the equator receiving as little as 23 W/m²) .

   Not surprisingly, these insolation changes with obliquity imprint on the spatial and temporal distribution of near-surface temperatures (Fig. 1, bottom): in the annual mean, temperatures at the equator decrease monotonically with obliquity from 295 K at 23.5° to 274 K at 85°, while polar temperatures increase from 268 K at 23.5° to 281 K at 85°. At summer solstices (Fig. 1, bottom), the summer pole becomes increasingly warmer, reaching 326 K at 85°, over 20 K warmer than the corresponding temperature at 23.5°.

   The entire evolution of insolation and near-surface temperatures throughout the year is shown in Fig. 2. Note how despite the very small thermal iner-
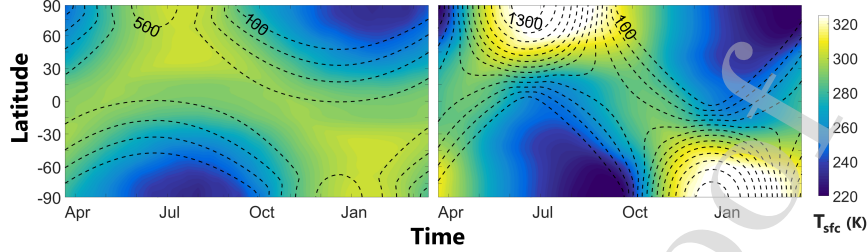
8

Figure 2: Near-surface temperatures (color contours, K) and shortwave incoming radiation (dotted lines, W/m^2) vs time for $23.5°$ (left) and $85°$ (right) obliquity with $\tau_{control}$. Radiation contours have intervals of 100 W/m^2, with the highest and lowest contours labeled.

tia of the lower boundary, near-surface temperatures lag insolation by about one month because of atmospheric thermal and dynamical inertia (e.g., Wei & Bordoni, 2018).

165   While these results are not surprising, there are aspects of the temperature distribution that are less obvious. In particular, the changes in near-surface temperature gradient between the winter and summer hemispheres as obliquity increases are much smaller than might be expected in radiative equilibrium given the dramatic insolation gradients at high obliquity. This suggests that
170 atmospheric energy transport plays a fundamental role in redistributing energy from regions of net energy input to regions of net energy deficit and in mitigating temperatures.

The meridional energy transport is given by:

$$< \overline{vh} > = \int_0^{P_s} \overline{vh} \, \frac{dp}{g} \tag{2}$$

where v represents the meridional flow, h the moist static energy (MSE) defined
175 as $h = c_p T + gz + L_v q$, which is comprised of dry enthalpy ($c_p T$, with isobaric specific heat c_p), potential energy (gz, with gravitational constant g) and latent energy ($L_v q$, with latent heat of vaporization L_v and specific humidity q). The bar represents a time and zonal mean. The total meridional energy transport

9

can be further decomposed as

$$< \overline{vh} > = < \overline{v}\overline{h} > + < \overline{v'h'} > \qquad (3)$$

with the first term on the right hand side representing the transport by the zonal
mean circulation and the second term representing the contribution by large-
scale eddies, which in an aquaplanet are exclusively transient eddies. These
components are shown in Fig. 3 for both the annual mean (top) and the northern
hemisphere (NH) summer solstice (bottom) for 23.5° and 85° obliquities.

The annual-mean energy transport in the 23.5° case shows features con-
sistent with Earth's energy transport, including poleward energy transport in
both hemispheres and maximum values of 2.9 PW around 30° N and S. Trans-
port by the Hadley cell dominates in the tropics, and transport by transient
eddies peaks in the extratropics, more than canceling the equatorward trans-
port by the indirect Ferrel cells. At 85°, total energy transport is still poleward
in both hemispheres, despite the reversed gradient in imposed insolation, but
much weaker than in the low obliquity case, with maxima of about 1.3 PW.
This transport is dominated at all latitudes by the mean transport, with eddy
transport being weaker and equatorward. That the transport is poleward (that
is, up the insolation gradient) in the high obliquity case suggests the existence
of a strong seasonality, which dominates the annual mean. It also emphasizes
the importance of resolving seasonal cycles in these more extreme planetary
regimes. This is a point we return to in the Discussion section.

At NH summer solstice, in the 23.5° case, the total energy transport is
southward in both hemispheres, which indicates, as expected, transport from
the summer (NH) into the winter (SH) hemisphere. Throughout the summer
hemisphere and at lower latitudes in the winter hemisphere, the transport is
dominated by the mean circulation. Eddy transport is significant only in the
winter hemisphere extratropics, and it is in fact negligible in the summer hemi-
sphere midlatitudes. At 85°, the solstice mean transport is much larger than
in the lower obliquity case and entirely effected by the mean circulation. This
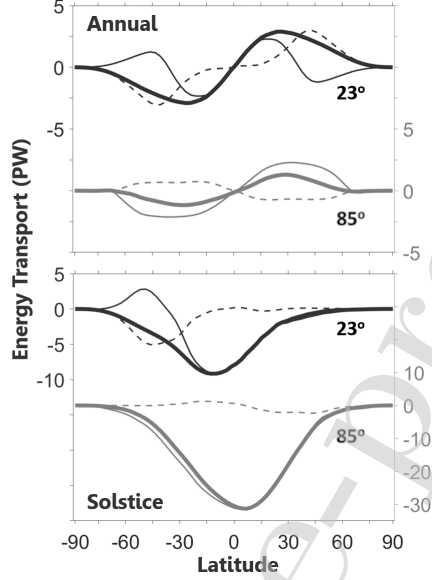is indicative of a solstice-mean Hadley circulation dominated by a strong cross-

10

Figure 3: Vertically integrated MSE transport (PW) for 23.5° (black) and 85° (gray) obliquities and $\tau_{control}$. Top figure shows annual mean and bottom shows NH summer conditions. Dashed lines indicate eddy, solid mean, and bold total (eddy + mean) components.

equatorial winter cell spanning a broad latitudinal range in both hemispheres (see Section 4). Somewhat surprisingly, eddy transport at solstice is negligible even in the winter hemisphere. It is hence clear that the weak annual mean transport is the result of much stronger solstice transports, which switch sign with season and hence mostly cancel out.

In Fig. 4, the total, mean and eddy transports are broken down into dry static energy ($c_p T + gz$) and latent energy ($L_v q$) components. For low obliquities, the dry static energy transport has the same sign as the MSE transport, because the atmosphere is stably stratified in a dry sense. The latent energy has oppositely signed transport (that is, northward in NH summer solstice), because moisture is primarily concentrated at lower levels and decreases rapidly with height. While the dry static and latent energy components largely cancel each other, the dry stratification wins out, giving rise to an overall southward transport.
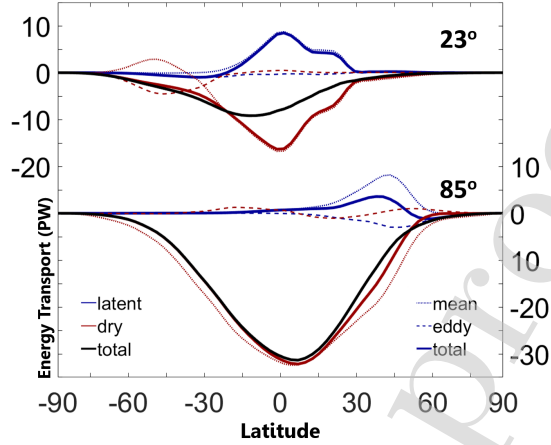
11

Figure 4: Vertically integrated MSE transport at NH summer solstice, broken down into dry component (gravitational + sensible) in red, and latent energy component in blue. Mean and eddy components are shown in dotted and dashed lines respectively, and totals are shown in bold.

Interestingly, in the high obliquity case, the transport is entirely dominated by the dry static energy component, with the latent energy being still opposite in sign but much smaller and nonnnegligible only in the ITCZ region. We find that at solstice, increasing obliquity consistently leads to a more dominant dry static energy transport for all cases, and a slight reduction of the latent energy transport. This can be seen in Fig. 5, where we show the vertically integrated cross-equatorial MSE transport at NH summer solstices (pentad 18) for all modeled obliquities. The decrease in latent heat transport occurs because the warmer and moister regions are progressively more and more confined to the summer pole as obliquity is increased, and contribute little to the overall transport.

The latent energy transport distribution shown in Fig. 4 also gives some insight into the precipitation patterns. At 23.5° obliquity, we see moisture converging (a negative slope in the flux) both near the equator and near 25° latitude, which correspond well to the two main convergence zones that can
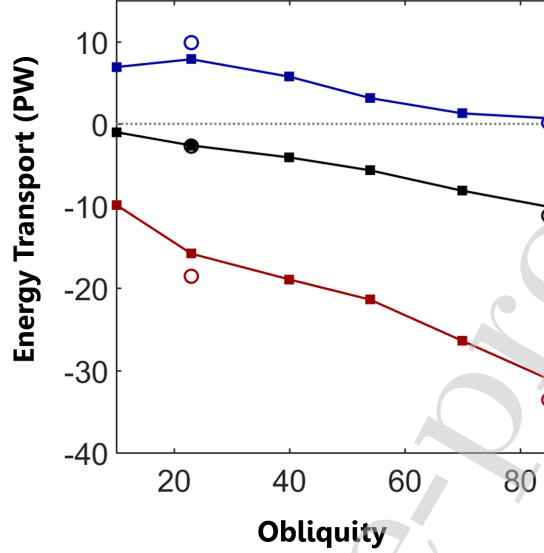
12

Figure 5: Cross-equatorial (average between 5°S and 5°N) MSE transport (black) at NH summer solstice, and its dry static energy (gravitational + sensible energy, red) and latent energy (blue) components for all obliquity values. $\tau_{control}$ and τ_{wv} results are shown with squares and open circles, respectively.

been seen in the tropical region at this time of the year (Fig. 6). At high obliquity, however, convergence is primarily centered at around 40° from the equator. While the low obliquity case is dominated by the mean transport, at high obliquity we see a competition between the mean and eddy terms. The
²⁴⁰ mean latent energy transport is northward, in the same direction as the low-level flow in the mean Hadley circulation, whereas the eddy transport is in the opposite direction, consistent with transport down the mean gradient, with maximum moisture values at the summer pole.

The relationship between moisture transports, and associated convergence,
²⁴⁵ and precipitation is made more apparent in Fig. 6, which shows near-surface winds and precipitation at 23.5° and 85° obliquities. As obliquity increases, there are consistent patterns of precipitation changes: 1) the tropical precipitation distribution shifts from a double ITCZ structure, with a near-equatorial
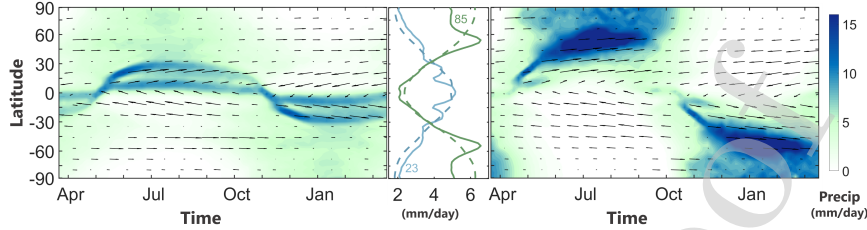
13

Figure 6: Precipitation (color contours, mm/day) and near-surface wind vectors vs time for 23.5° (left) and 85° (right) obliquity with $\tau_{control}$. The center panel shows annual mean values of precipitation (solid lines) and evaporation (dashed lines), also in mm/day.

secondary peak and a subtropical primary peak, to a single ITCZ structure peak-
²⁵⁰ ing at progressively higher latitudes; and 2) high latitude precipitation outside of the ITCZ also increases. Mechanisms behind these changes will be discussed in Section 5.

Another feature of interest in the precipitation patterns at all obliquities is the absence of a storm track, that is a band of enhanced precipitation in
²⁵⁵ the winter hemisphere extratropics. This raises the question of to what extent this might be associated with the lack of eddy activity. To more quantitatively answer this question, in Fig. 7 we show the vertically integrated eddy kinetic energy (EKE) at NH summer solstice. We see that, as obliquity increases, EKE decreases because of decreased lower-level temperature gradients in the winter
²⁶⁰ hemisphere. Also, though EKE is relatively large at Earth's obliquity, there is still no obvious precipitation storm track because of very low temperatures and, hence, very little available moisture. Notice how this is not representative of Earth's present-day climate because of the very shallow mixed layer depth, which allows for more extreme temperature variations than what is seen on
²⁶⁵ Earth.

4. The Hadley Cell

The surface climate described in the previous section is strongly influenced by the large-scale circulation and associated moisture and energy transports. Thus,
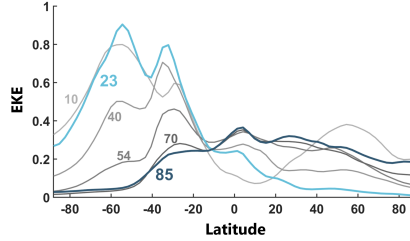
14

Figure 7: Vertically integrated eddy kinetic energy (up to $\sigma = 0.23$) in MJ/m^2 for all obliquities at NH summer solstice (pentad 18).

it is important that we more explicitly quantify the changes in the Hadley cell

²⁷⁰ as obliquity is increased. Solstitial Hadley cells in aquaplanet simulations with shallow mixed layer depths, and their relevance to monsoonal cross-equatorial circulations in the Earth's atmosphere, have been previously discussed in the literature (e.g., Bordoni & Schneider, 2008; Merlis & Schneider, 2010; Faulk et al., 2017; Zhou & Xie, 2018). Similarly to those studies, we find that in

²⁷⁵ the solstice seasons for Earth-like obliquity, the Hadley cell is dominated by a solstitial pattern, with a strong cross-equatorial winter Hadley cell and a negligible summer cell. This can be seen in Fig. 8, which shows the overturning circulation at NH summer solstice for 23.5 and 85° obliquity, together with the distribution of zonal winds and eddy momentum flux divergence. The small

²⁸⁰ inertia of the shallow mixed layer depth makes it possible for the lower-level MSE to adjust rapidly on seasonal time scales, allowing the cell to intensify and expand rapidly into the summer hemisphere following the lower-level MSE maximum, which can move to around 30 degrees off the equator for Earth-like conditions (e.g., Privé & Plumb, 2007; Bordoni & Schneider, 2008). As the cir-

²⁸⁵ culation becomes cross equatorial and more strongly approaches conservation of angular momentum, upper-level easterlies develop over the tropics spanning almost the entire cell extent (Lindzen & Hou, 1988). Eddy momentum flux divergence is weak throughout the cell extent thanks to the shielding effect of the upper-level easterlies and, in fact, only affects the Hadley cell in its de-

15

290 scending branch (e.g., Schneider & Bordoni, 2008; Bordoni & Schneider, 2008). Near the surface, westerlies develop in the summer hemisphere from around the equator up to the circulation's poleward boundary (Fig. 6), as friction on the westerly flow balances the Coriolis force on the poleward meridional flow. As obliquity is increased, and so are the latitude of the maximum solar forcing and 295 the summer pole-to-equator temperature gradient, the cross-equatorial circulation broadens and intensifies, upper-level easterlies strengthen and prevail over an increasing portion of the cross-equatorial cell, and eddy momentum flux divergence is significant only in its descending branch. As the circulation becomes increasingly cross equatorial, its ascending branch broadens, consistent with the 300 precipitation patterns shown in Fig. 6. It is however important to note how, while much broader than what seen in the $23.5°$ case, the winter cross-equatorial cell in the $85°$ case is not truly global, with most of the circulation mass flux being confined within 60 degrees of the equator. As we discuss in the following section, energy and angular momentum constraints prevent the circulation from 305 extending up to the latitude of maximum temperature and MSE (e.g., Hill et al., 2019; Guendelman & Kaspi, 2018) and the precipitation in the polar region is not associated with the ascending branch of the mean overturning circulation.

It is also worth noting how these overturning patterns confirm the overall lack of a significant Ferrel cell at solstice in the winter hemisphere. We see a 310 weak winter Ferrel cell at $10°$ (not shown) and $23.5°$ obliquity (Fig. 8), but it disappears at higher obliquities. This is at odds with the simulations in Ferreira et al. (2014), who argue that the single cell dominating the overturning circulation in their high obliquity simulations results from a merging of the Ferrel cell with a Hadley cell driven by reversed meridional temperature gradients. In the 315 absence of ocean dynamics, at least in this model with our chosen parameters, the resulting cross-equatorial Hadley cell becomes so strong that the associated energy transport, combined with moisture effects, smoothens out temperature gradients in both hemispheres and prevents any significant eddy activity. This is also consistent with the absence of any reversal in the meridional PV gradient 320 in the higher obliquity runs (not shown).
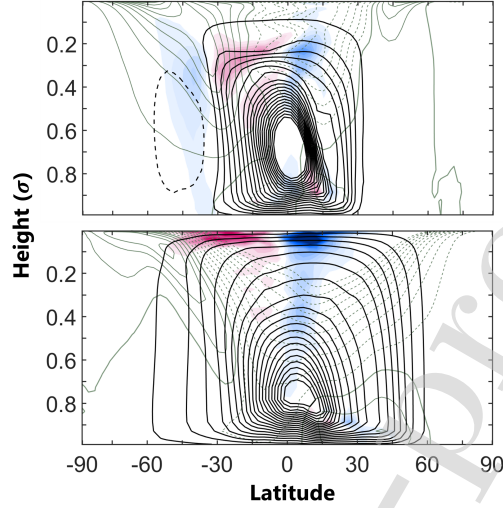
16

Figure 8: Hadley Cell at NH summer solstice for 23.5° (top) and 85° (bottom). Streamfunction is shown in solid black lines (contour intervals of 25×10^9 kg/s), eddy momentum flux divergence, $\nabla \cdot (\overline{u'v'}cos\phi)$, in color contours (contour intervals of 5×10^{-6} m^2/s^2) and zonal wind in gray lines (contour intervals of 10 m/s, with solid (dashed) for positive (negative) values).

5. Hydrological Cycle

5.1. ITCZ

In its simplest definition, the ITCZ is the region of maximum zonal mean tropical precipitation, associated with the ascending branch of the Hadley cell

₃₂₅ (Kang et al., 2008; Kang et al., 2009). However, when applied to diagnosing the ITCZ position from our simulations, any metric based on the detection of the absolute precipitation maximum presents some challenges. As can be seen from Fig. 6, tropical precipitation can have a double, rather than a single, peak structure: in addition to the precipitation peak associated with the ascending

₃₃₀ branch of the Hadley cell, especially for low obliquities, there exists a secondary precipitation band in the summer hemisphere that remains close to the equator and, at times, can become the locus of most intense rainfall. Additionally, as

17

obliquity increases, not only does the ITCZ shift to higher latitudes, but it also becomes broader and somewhat less defined.

335   To account for these difficulties, here we detect the ITCZ position using three different methods that exist in the literature: 1. Latitude of maximum precipitation $\phi_{P_{max}}$; 2. Precipitation centroid (Frierson & Hwang, 2012), defined as the center of mass of the area-integrated precipitation between $\pm\phi_e$:

$$\int_{-\phi_e}^{\phi_C} P\cos(\phi)d\phi = \int_{\phi_C}^{\phi_e} P\cos(\phi)d\phi; \qquad (4)$$

where we have chosen symmetric integration limits, prescribed based on a visual
340 inspection to include the entire precipitation distribution associated with the Hadley cell. The values vary smoothly from 30° to 77° latitude as obliquity increases from 10° to 85°. This cutoff becomes increasingly arbitrary for the higher obliquity cases where additional polar precipitation can blend into the ITCZ, but results are robust to different choices of ϕ_e. 3. An integer power N
345 of area-integrated tropical precipitation (Adam et al., 2016):

$$\phi_N = \frac{\int_{\phi_a}^{\phi_b} \phi[\cos(\phi)P]^N d\phi}{\int_{\phi_a}^{\phi_b} [\cos(\phi)P]^N d\phi}. \qquad (5)$$

As discussed in Adam et al. (2016), higher N values provide estimates of the ITCZ that are close to the actual precipitation maximum, but are less sensitive to the horizontal resolution of the precipitation output. We choose N = 10, $\phi_a = -90°$ and $\phi_b = 90°$.

350   Values of these three different ITCZ metrics are shown in Fig. 9 for all simulations. Note that here we show only the maximum latitudinal reach of ϕ_N, which occurs at different times for the different obliquity values. For instance, in the 85° simulation the ITCZ reaches its maximum poleward excursion one month later than what is seen in the 10° case. The remaining metrics in
355 Fig. 9 are shown at the time of maximum ϕ_N. These three precipitation-based metrics tend to agree well with each other at low obliquities; as obliquity is

18

increased, however, we see that, while $\phi_{P_{max}}$ and ϕ_N are generally collocated, they become increasingly separated from ϕ_C (by about 10° in the larger obliquity cases). This reflects an overall widening of the ITCZ. While primarily due

360 to a widening of the Hadley cell ascending branch, the ITCZ broadening also results from changes in the contribution of large-scale eddies to the moisture budget (discussed in the following subsection). More specifically, as poleward temperature and moisture gradients in the summer hemisphere increase with increasing obliquity, large-scale eddies acting down the mean moisture gradient

365 diverge moisture from the higher latitudes and converge it to lower latitudes, right on the equatorward side of the ITCZ (Fig. 10). Correspondingly, the contribution to the total precipitation from large-scale condensation (that is, the one arising from grid-scale saturation rather than that arising from sub-grid convective scale motion) increases in this region, as will be discussed in

370 Section 5.2.

Tracking changes of just the ITCZ's maximum latitudinal reach facilitates comparison between different simulations in Fig. 9, but hides some of the changes in timing that occur for higher obliquities and how different metrics capture the corresponding changes in precipitation patterns. In Fig. 11, we zoom into

375 the NH summer for 85° obliquity. As it can be seen, the poleward shift of the ITCZ occurs very smoothly during the start of the summer season, during which time the three ITCZ position metrics agree well with each other. At the end of summer, however, tropical precipitation decreases rapidly in the summer hemisphere, before switching to the opposite hemisphere and intensifying there,

380 as the associated warm season begins (Fig. 6). The three ITCZ position metrics capture different aspects of these changes in precipitation patterns: the centroid misleadingly portrays a smooth transition into the opposite hemisphere; ϕ_N briefly moves to the latitudes of the very weak near-equatorial precipitation zone, and $\phi_{P_{max}}$ rapidly shifts to polar latitudes, where a local precipitation

385 peak develops (as discussed more in detail in Section 5.2).

With these measures of the ITCZ reach in mind, it is of interest to test the applicability of other diagnostics that are not based on precipitation and are tra-

19

ditionally used for Earth's ITCZ. One very common diagnostic used to predict the location of maximum tropical precipitation is the maximum in near-surface

390   MSE. As discussed in Sobel et al. (2007), local thermodynamic constraints would predict maximum convection, and with it maximum lower-level convergence and precipitation, to occur near maximal surface temperatures. When combined with considerations for an angular momentum conserving overturning circulation (Lindzen & Hou, 1988), and quasi-equilibrium theories of moist convection

395   (Emanuel et al., 1994), local controls would suggest the ITCZ's location be just equatorward of the near-surface MSE maximum (Emanuel et al., 1994; Privé & Plumb, 2007; Bordoni & Schneider, 2008).

   The location of the near-surface MSE maximum for each obliquity at the time of the maximal ITCZ excursion is plotted in Fig. 9 as the dark shaded

400   area. At obliquities larger than 40°, the MSE maximum moves to the pole, following the maximum of solar insolation. And yet, the precipitation maximum does not follow. This emphasizes how the maximum lower-level MSE is not always a good indicator of the ITCZ when planetary regimes other than Earth's are being considered (e.g., Faulk et al., 2017; Hill et al., 2019). As the MSE max-

405   imum moves outside of the tropics, convective heating anomalies are no longer communicated to remote regions through gravity waves and horizontal temperature gradients are no longer constrained to be small outside of the boundary layer (Sobel & Bretherton, 2000). In other words, convection can no longer self-organize in a coherent ITCZ over the MSE maximum and suppress convection

410   elsewhere if the MSE maximum is removed from the tropics (e.g., Faulk et al., 2017). As will be discussed in Section 5.2, the region of high-latitude MSE maximum is correlated with polar convective activity; this however remains a local process and is not embedded within the ascending branch of the Hadley cell. Theoretical arguments based on axisymmetric Hadley cell theory as to

415   why lower-level MSE might not always be predictive of the poleward extent of cross-equatorial Hadley circulations have recently been discussed by Hill et al. (2019).

   Another commonly used metric of the ITCZ position for Earth's climate is

20

the energy flux equator (EFE), defined as the latitude at which the vertically

420 integrated meridional MSE flux vanishes (Kang et al., 2008). In particular, the vertically integrated atmospheric energy budget in recent years has provided the theoretical framework to understand shifts in the ITCZ induced by remote forcing, as part of the anomalous energy fluxes by the Hadley cell needed to restore energy balance (e.g., Bischoff & Schneider, 2014; Frierson & Hwang, 2012).

425 Under Earth's conditions, where the asymmetry between the two Hadley cells is small, their dividing boundary approximately coincides with the latitude at which the vertically integrated energy transport vanishes. That is to say, the EFE is well defined. As the Hadley cell becomes more hemispherically asymmetric, with a strong, broad and intense winter cell and vanishing summer cell

430 (e.g., Faulk et al., 2017; Wei & Bordoni, 2018), this boundary becomes ill-defined and in fact does not always correspond with a change of sign in energy or mass transport. For these reasons, here we identify the EFE as the latitude at which the energy transport by the cross-equatorial Hadley cell reduces to 5% of its maximum value. As shown in Fig. 9, being a measure of the dividing bound-

435 ary of the two Hadley cells (or of the poleward extent of the cross-equatorial winter cell), the EFE overestimates the ITCZ position at all obliquities. Yet, it performs better than the MSE maximum, and, at high obliquities, it is only separated by about $10°$ from the ITCZ.

Given that the EFE and, at least for Earth-like conditions, the lower-level

440 MSE maximum are a metric of the dividing boundary of the two Hadley cells, rather than of the ITCZ position itself, it is also of interest to explore how more direct measures of the circulation extent compare to these other indicators. Here we take two approaches: we first estimate the poleward extent of the cross-equatorial Hadley cell directly from the simulated overturning mass

445 streamfunction, and then we use estimates based on the angular-momentum conserving theory of Hadley cells forced by off-equatorial heating (e.g., Held & Hou, 1980; Lindzen & Hou, 1988).

The simulated Hadley cell edge, which is shown in light gray shading in Fig. 9, much like the EFE, is difficult to define for the high obliquity cases

21

450 since there is no reversal in the sign of the streamfunction. Hence, here we computed it as the latitude at which the streamfunction decreases to 5% of its maximum values. We also use a cosine factor to account for Earth's geometry, as was first done by Singh (2019), such that $\Psi(\phi)\cos\phi = 0.05\Psi^*\cos\phi^*$ where ϕ^* is the latitude where the streamfunction maximizes, and Ψ^* is the maximum

455 streamfunction value.

The theoretical angular momentum conserving Hadley cell extent of Lindzen & Hou (1988) is obtained utilizing an assumed radiative-equilibrium temperature profile of the form:

$$\theta_{re} = \theta_o\Big\{1 + \frac{\Delta_H}{3}[1 - 3(\sin\phi - \sin\phi_o)^2]\Big\}. \tag{6}$$

Note that Eq. 6 is not the GCM forcing; it is the vertically averaged forcing

460 used in Lindzen & Hou (1988), which allows for numerical simplicity. θ_o is a reference temperature (300K), ϕ is latitude, ϕ_o is the latitude of maximum forcing, here interpreted as obliquity, and Δ_H is the fractional change of potential temperature. Values of Δ_H were calculated based on vertically integrated potential temperatures at equinox from the model output, as per the Lindzen &

465 Hou (1988) definition of Δ_H, and ranged from 0.21 to 0.23.

The solution assumes that the regions beyond the Hadley cell are in radiative equilibrium, with temperatures satisfying Eq. 6, while within the Hadley cell, temperatures are in gradient-wind balance with the angular momentum conserving winds, yielding:

$$\theta(\phi) = \frac{-\Omega^2 a^2}{2gH}\theta_o\frac{(\sin^2\phi - \sin^2\phi_1)^2}{\cos^2\phi} + \theta(\phi_1) \tag{7}$$

470 where ϕ_1 is the latitude of the dividing boundary between the southern and northern cell, and H is the tropospheric height (here taken as 12 km). By requiring conservation of energy in the Hadley cell region to either side of the ITCZ, and continuity of temperature at the Hadley cell edges, it is possible to solve for ϕ_1, shown in red in Fig. 9.

475 The simulated Hadley cell edge follows a trend similar to the angular momentum conserving limit, which expands with obliquity but remains constrained

22

and does not extend into the polar regions. The agreement between estimates of the cell extent based on the Lindzen & Hou (1988) model and those directly derived from the simulations is not surprising, as strong cross-equatorial circu-
480 lations tend to approach conservation of angular momentum, at least in their ascending and upper branches, even when eddy fluxes in the winter hemisphere are not negligible (e.g., Schneider & Bordoni, 2008).
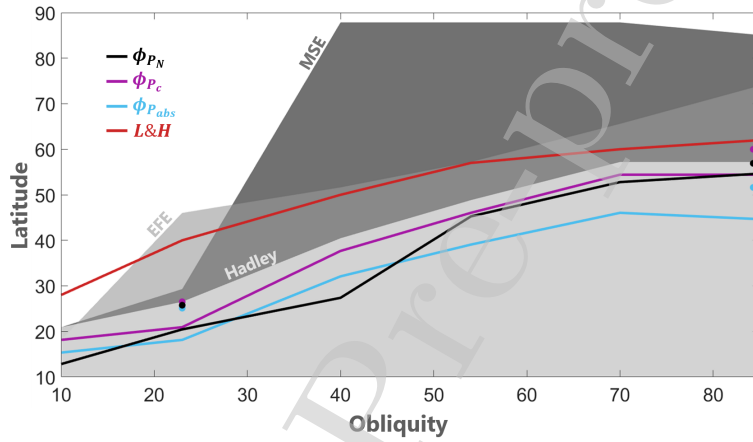

Figure 9: Maximal off-equatorial ITCZ reach during NH summer vs obliquity: ϕ_N (black), ϕ_C (magenta) and $\phi_{P_{max}}$ (blue). Gray shading indicates latitude of the lower-level MSE maximum (dark), of the EFE (medium) and the Hadley cell extent (light). The red line shows theoretical predictions of the Hadley cell extent from angular momentum conserving theory. The maximum ITCZ reach is also shown for τ_{wv} simulations, using markers of the same colors.

5.2. Polar precipitation

Beyond the ITCZ, there is an increasing tendency for local precipitation
485 maxima to occur at high latitudes with increasing obliquity (Fig. 6). A close up of the polar region for 85° obliquity is shown in Fig. 12, with contours of the large-scale precipitation. Because the summer pole at high obliquities is where lower-level MSE maximizes, local convective activity does contribute significantly to the polar precipitation during the peak of the summer. Inter-
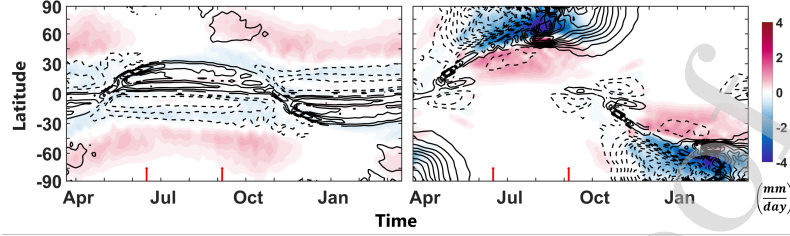
23

Figure 10: Time evolution of the eddy moisture flux convergence (shading, mm/day) and net precipitation (line contours, mm/day). Red arrows on the x-axis indicate the pentads of the time slices in Fig. 13.

estingly, however, at the end of the summer, when temperatures are starting to decrease rapidly, large-scale condensation increases sharply as convective activity declines. What determines this rapid increase in large-scale precipitation?

To answer this question, we analyze the vertically integrated moisture budget, which relates the net precipitation $(P - E)$ to the convergence of moisture flux into the atmospheric column and water vapor storage. Further decomposing the water vapor flux into mean and eddy components, the moisture budget becomes:

$$(\overline{P} - \overline{E}) = -\nabla . <\overline{q}\,\overline{\mathbf{u}}> -\nabla . <\overline{q'\mathbf{u}'}> - \partial_t <\overline{q}> \tag{8}$$

where $< \cdot >$ indicates a mass-weighted vertical integral and $\overline{(\cdot)}$ indicates a long term pentad average. The three terms on the right-hand side of Eq. 8 represent the mean moisture flux convergence, the eddy moisture flux convergence and the storage terms, respectively. Note that storage is the rate at which water vapor is stored in the atmospheric column (also called precipitable water).

The panels in Fig. 13 show the moisture budget and contributions by each component for two different time slices, with one slice at peak summer and one in the fall. The specific times at which the slices were taken are indicated with red arrows in Fig. 10, which also shows the eddy moisture flux convergence over time. For 23.5° obliquity, we see a balance that is typical of the tropics: the mean moisture flux convergence produces most of the precipitation, with very
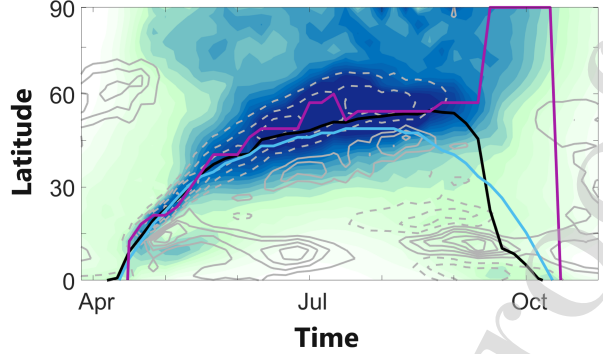
24

Figure 11: ITCZ location over time for $85°$ obliquity and $\tau_{control}$, during NH summer. Line colors match definitions in Fig. 9 with ϕ_N (black), ϕ_C (blue) and $\phi_{P_{max}}$ (magenta). Color contours show precipitation with the same color scheme as Fig. 6, and gray contours show near surface convergence $(\partial v / \partial y)$ where positive (negative) values are shown as solid (dashed) lines.

little contribution from the eddies and an insignificant storage term.

⁵¹⁰   At higher obliquities, we see that this balance is no longer valid. For $85°$ obliquity the mean moisture flux convergence still dominates over the eddies in the tropics, but neither dominates at the summer pole. It is interesting to see how at the peak and end of the warm season, the summer pole experiences, respectively, large net evaporation $(E > P)$ and net precipitation $(P > E)$ ⁵¹⁵ which are not balanced by moisture flux convergence by either the mean or eddy motions. It is in fact the moisture storage term, which is usually negligible at Earth's obliquities, that takes a dominant role at these times and latitudes.

During the summer at high obliquities, as temperatures increase, so does the water holding capacity of the atmosphere, and hence excess evaporation ⁵²⁰ is primarily stored in the atmospheric column as precipitable water. At the end of summer, temperatures drop rapidly (Fig. 2) and the stored water vapor condenses and precipitates out. Storage increases monotonically with obliquity, as can be seen in Fig. 14.

It is important to note how these results are not dependent on the specific ⁵²⁵ choice of the optical depth: while the specific value of the optical depth at
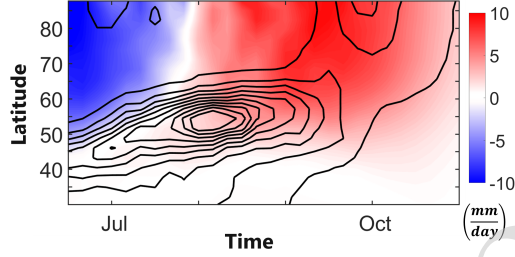
25

Figure 12: Close-up of polar large-scale precipitation (black contours) around the NH warm season for the 85° simulation and $\tau_{control}$ in intervals of 2 mm/day. Color contours shows the evolution of storage term $-<\partial q/\partial t>$ for this region, also in mm/day.
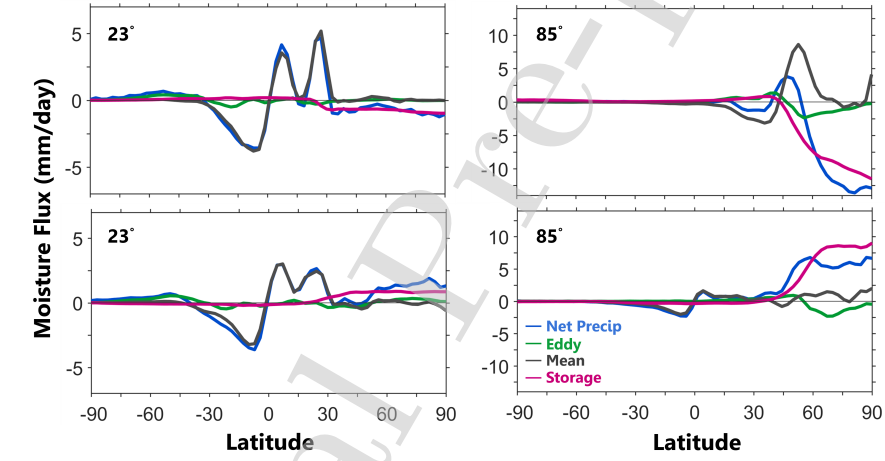

Figure 13: Moisture budget decomposition at two times of the seasonal cycle for 23.5°(left) and 85°(right) obliquity and $\tau_{control}$, with net precipitation in blue, mean moisture flux convergence $(-\nabla.<\overline{u}\,\overline{q}>)$ in dark gray, eddy moisture flux convergence $(-\nabla.<\overline{q'u'}>)$ in green and storage $(-\partial_t <q>)$ in pink. All values are in mm/day.

the poles influences some quantitative aspects of the simulated seasonal cycle, the behavior of the moisture budget remains qualitatively the same, driven by the rapid changes in temperature experienced at the poles. Hence, storage, which is usually neglected in studies of the Earth's hydrological cycle, becomes a leading-order term in climates with more extreme seasonal cycles.
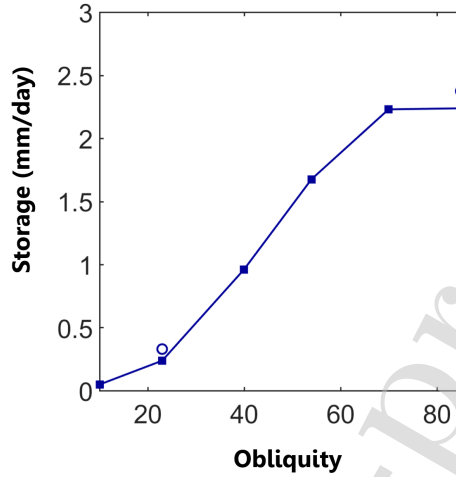
26

Figure 14: Peak value of water vapor storage ($- <\partial q/\partial t>$, averaged from 60 to 90 degrees latitude) in mm/day for various obliquities. Values for $\tau_{control}$ are indicated with squares, and values for τ_{wv} are shown with circular markers.

5.3. Equatorial secondary maximum

In the lower obliquity scenarios, tropical precipitation has a double ITCZ structure, with a secondary precipitation band in the summer hemisphere that remains at the same near-equatorial location throughout the summer season.
535   This near-equatorial convergence zone can at times rival the ITCZ in precipitation values and even be the absolute precipitation maximum, with values greater than the ones in the ITCZ (Fig. 6). Interestingly, this feature is largely absent at high obliquities, with the result that in the annual mean the near-equatorial region has negative net precipitation (that is, evaporation exceeds precipitation)
540   unlike what is seen on Earth (center panel, Fig. 6).

This near-equatorial precipitation maximum is collocated with strong ascending motion in latitudes where the return flow of the lower branch of the cross-equatorial Hadley circulation rises above the boundary layer. This happens well equatorward of the ascending branch, which is close to its poleward
545   boundary. This "jumping" behavior has been shown to be ubiquitous in ide-

27

alized simulations of cross-equatorial Hadley circulations (e.g., Wei & Bordoni, 2018). But unlike previous studies, in our simulations the "jump" is located in the summer rather than the winter hemisphere (e.g., Pauluis, 2004; Privé & Plumb, 2007).

The dynamics of this near-equatorial jump has been described in detail by Pauluis (2004). In short, strong virtual temperature gradients are necessary for strong meridional flow in the boundary layer around the equator, where the Coriolis parameter is negligible. If that flow cannot be accommodated in the boundary layer, either because of weak virtual temperature gradients or a too shallow boundary layer, the return flow is prevented from occurring in the boundary layer and must in fact do so in the free troposphere.

In order to explore to what extent differences in the near-equatorial and near-surface virtual temperature (and hence pressure) gradients can explain the presence or absence of this secondary precipitation maximum in the low and high obliquity cases, respectively, we use the boundary layer momentum equations introduced by Pauluis (2004). For an axisymmetric model, with a homogenized mixed layer of constant depth (D_{ml}) and constant virtual temperature gradient throughout the layer, Pauluis (2004) shows that the linearized boundary layer momentum equations in steady state become:

$$fv_b - \tau^{-1}u_b = 0 \tag{9}$$

$$fu_b + \frac{1}{a}\frac{\partial \Phi}{\partial \phi}\Big|_b + \tau^{-1}v_b = 0 \tag{10}$$

where surface friction has been parameterized through a frictional dissipation time scale τ. From Eqs. 9 and 10, we can solve for the meridional flow v_b.

$$v_b = \frac{-\tau}{(\tau^2 f^2 + 1)}\frac{1}{a}\frac{\partial \Phi}{\partial \phi}\Big|_b \tag{11}$$

with

$$\frac{1}{a}\frac{\partial \Phi}{\partial \phi}\Big|_b = -fu_f - \frac{D_{ml}}{2H_r}\frac{R}{a}\frac{\partial T_v}{\partial \phi} \tag{12}$$

28

where H_r is the atmospheric scale height, R is the ideal gas constant, a is the
planetary radius, T_v is the virtual temperature and u_f is the zonal velocity right
above the mixed layer.

Right at the equator, where the Coriolis parameter is equal to zero, the
cross-equatorial meridional flow is entirely driven by the near-surface pressure,
and hence, temperature gradient. More generally, free-tropospheric geopoten-
tial gradients (which are geostrophically balanced by the term $-fu_f$ in Eq. 12)
are weak in the near-equatorial region and hence inefficient at driving any cross-
equatorial flow. Hence, the meridional component in the Hadley cell return flow
nearby the equator is primarily determined by the near-surface virtual temper-
ature gradient, which needs to be positive (negative) to sustain the poleward
flow in the NH (SH) during summer, as required by mass balance in a cross-
equatorial circulation with ascending branch in the summer hemisphere. In
Fig. 15 we show the meridional virtual temperature gradients (color contours)
from the 23.5° and 85° simulations with $\tau_{control}$. In the 23.5° obliquity simula-
tion, it is evident that the near-surface meridional temperature gradient changes
sign in a narrow region which well coincides with the near-equatorial precipita-
tion band. The lower-level poleward flow cannot cross this region at low levels,
and hence, has to jump out of the boundary layer, creating lower-level conver-
gence and divergence, respectively, on the upstream and downstream side of it.
This behavior is also apparent from the streamlines in Fig. 8.

The absence of the near-equatorial precipitation maximum at higher obliqui-
ties is partly explained by differences in the seasonal evolution of the near-surface
virtual temperature gradients. More specifically, the near-surface temperature
gradient (Fig. 15, right panel) remains primarily positive throughout the warm
season, with the exception of short times at its beginning and end. These are
also the only times when near-equatorial precipitation is nonnegligible (Fig. 6,
right panel).

While not featuring a reversal in the meridional temperature gradient, the
85° simulation still features an inflection point at around 8 degrees on the sum-
mer side of the equator, which would also prevent any poleward flow crossing
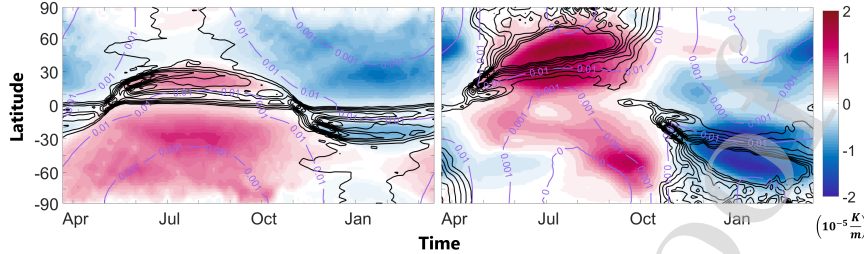
29

Figure 15:   Near-surface meridional virtual temperature gradients (color contours, 10^{-5} K/m), precipitation (black line contours from 5 to 12 mm/day) and near-surface specific humidity (gray line contours, kg/kg) vs time for $23.5°$ (left) and $85°$ (right) obliquity with $\tau_{control}$.

that region of the boundary layer and would result in a region of lower-level convergence. This inflection point is collocated with the equatorial precipitation maxima at the start and end of summer, and persists throughout the summer even when near-equatorial precipitation is nearly absent (Fig. 15). This suggests that reasons other than just the temperature gradients are responsible for the different precipitation patterns in the low and high obliquity cases. Not surprisingly, the availability of moisture also plays a very important role. For low obliquities, the jumping occurs in regions with still relatively high lower-level moisture and MSE. Latent heat release in such moist ascent partially compensates the adiabatic cooling and results in a decrease in gross moist stability, which leads to deep ascent (Pauluis, 2004). For obliquities larger than $54°$, MSE and moisture maxima move rapidly away from the equatorial region into higher latitudes, with the lower latitudes being relatively cold and dry throughout the warm season. In this case, any ascent that occurs in this region is effectively dry and, in the absence of circulation-moist convection feedbacks, remains more shallow, as is also evidenced in the flatter streamlines of the return flow in the high obliquity case shown in Fig. 8.

In the Earth's literature, debate remains somewhat open as to whether tropical precipitation is more strongly controlled by thermodynamic or dynamic

constraints (e.g., Sobel et al., 2007). Thermodynamic theories emphasize the
importance of local temperature and moisture, with precipitation and convergence being primarily collocated with SST and MSE maxima (e.g., Neelin & Held, 1987; Sobel & Bretherton, 2000; Privé & Plumb, 2007). Dynamic theories instead consider the boundary layer momentum budget to determine the region of stronger lower-level convergence and hence precipitation (e.g, Lindzen & Nigam, 1987; Pauluis, 2004). Our simulations suggest that both thermodynamic and dynamic arguments can provide powerful constraints on the tropical precipitation distribution. They also emphasize how well-accepted theories for studies of the Earth's hydrological cycle need refinement when applied to more exotic climates (e.g., Hill et al., 2019).

6. Discussion

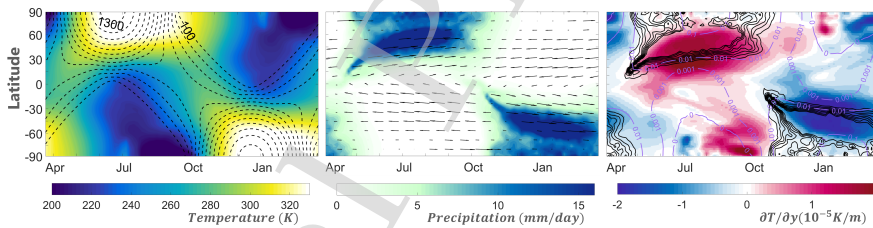### 6.1. Sensitivity to optical depth formulation

Figure 16: Same as Fig. 2 (left), Fig. 6 (center) and Fig. 15 (right), for a simulation with 85° obliquity and τ_{wv}.

The results discussed so far are all based on simulations where the longwave optical depth is only a function of pressure, but constant in latitude. Importantly, while the vertical structure of the optical depth has been designed to mimic separately the effects on the atmospheric opacity of a well-mixed CO_2-like absorber and of a bottom-heavy water vapor-like absorber (Eq. 1), there is no active water vapor feedback, in that the optical depth is not a function of the simulated water vapor. Given our emphasis on seasonal cycles, it is natural to wonder if and to what extent an active water vapor feedback would change

31

any of the results discussed above. To address this question, here we briefly discuss simulations where we introduce a crude representation of the water vapor feedback. Following Merlis & Schneider (2010), the optical depth is modified as:

$$\tau(p) = \tau_o \left(\frac{p}{p_0} \right) + \tau_{o_{wv}} \left(\frac{p}{p_0} \right)^4 \tag{13}$$

where $\tau_{o_{wv}}$ is not a specified constant but is the vertically integrated specific humidity, divided by an empirical constant (in this study 98 Pa) chosen so that $\tau_{o_{wv}}$ remains order one. τ_o is adjusted to a value of 1.39 so that the Earth-like 23.5° obliquity simulation yields a global and annual mean surface temperature approximately the same as that of the control simulation (± 0.1 K) . The same value is used for the 85° simulation discussed below.

At 23.5°, the differences in near surface temperatures are concentrated at the poles, with warmer summers ($\Delta T \leq 15$ K, with Δ indicating the difference between the water vapor and the control simulations) and colder winters ($\Delta T \geq -35$ K), and an overall warmer (by 2 to 7 degrees) equatorial region. Maybe not surprisingly, given the more extreme seasonality, in the 85° obliquity case, an active water vapor feedback produces significantly warmer (colder) temperatures at the summer (winter) poles, with differences up to 40 K relative to the control simulation (Fig. 16, left). Interestingly, the equatorial region is colder near the surface, with $\Delta T \approx -14$ K, and global annual mean temperature differences are small.

Despite these nonnegligible differences in surface temperature, all features of high-obliquity climates we discussed in previous sections remain qualitatively similar (Fig. 16, center). Some differences worth noting are: slightly poleward-shifted ITCZ (and associated metrics in Fig. 9), and absence of near-equatorial precipitation (Fig. 16, center) primarily explained by the absence of an inflection point in the near-surface virtual temperature (Fig. 16, right). Therefore, this suggests our results are robust regardless of optical depth meridional structure.

6.2. Seasonal cycle vs annual mean simulations

High obliquity planets have a stronger seasonal cycle of insolation than their low obliquity counterparts. Especially in a planet without an active ocean,

670 whose surface has a low heat capacity like the one modeled in this study, this results in more extreme temperatures and strong seasonal phenomena that are of leading order and yet are not captured in a model forced with annual mean insolation.

While this may appear to be an obvious statement, it merits emphasis in

675 the field of planetary sciences. As we work towards coarse characterizations of planetary climates of more distant planetary bodies, for which we have limited data, it may be tempting to focus exclusively on annual mean conditions. And yet, this may hide seasonal atmospheric responses that shape in fundamental ways the planetary climate.

680 Simple energy balance considerations already provide clues on how ignoring seasonally varying insolation might introduce nonnegligible errors in the estimate of the meridional distribution of the annual mean surface temperature. If we assume the planet behaves as a blackbody, energy balance requires the absorbed shortwave radiation be balanced by the outgoing longwave radiation

685 as $S = \sigma T^4$. Because the outgoing longwave is a strongly nonlinear function of temperature, it is clear that the annual mean surface temperature at each latitude in response to annual mean forcing will be different from the one obtained by annually averaging the response to seasonally varying forcing, with differences in the two increasing as seasonal variations increase.

690 We have in fact conducted simulations where insolation is kept at its annual mean value. Differences in the meridional distribution of the annual mean temperature with and without a seasonal cycle of insolation are shown in Fig. 17 for the 23.5° and 85° obliquity cases. Notice how temperatures in the annual mean simulations are not only higher, but also feature higher pole-to-equator

695 temperature contrast.

The discussion in the previous sections also makes clear how the planetary climate is dominated by seasonally varying phenomena that are not captured

33

in simulations with annual mean forcing, first and foremost the Hadley circulation. In fact, as obliquity increases and the pole-to-equator insolation (and

700   temperature) gradient in the annual mean reverses (Fig. 1 and 17), the Hadley cells reverse, with rising motions in the subtropics and descending motion at the equator (not shown). While overturning in a direction opposite to the one seen at Earth's obliquities, these cells are still thermally direct cells, with air in the warmer subtropics rising and air in the colder equator sinking. However, when a

705   seasonal cycle is resolved, the annually averaged overturning (and associated energy transport) is inconsequential, as the atmospheric circulation is dominated by seasonally-reversing, strong and broad cross-equatorial Hadley circulations. These circulations effect significant energy transport from the warm summer hemisphere to the cold winter hemisphere, leading to a much smaller annual

710   mean pole-to-equator temperature gradient than what is seen in the annual mean simulation (Fig. 17).

Other seasonal phenomena that are not captured in annual-mean simulations pertain to the hydrological cycle in polar regions, where seasonal storage effects are nonnegligible at high obliquities.

715   In summary, for a high obliquity planet with moderate-to-low surface heat capacity (and thus, strong seasonal cycles), modeling the atmospheric behavior without the seasonal cycle is not only a matter of oversimplification, but could result in errors that would make climate characterizations and habitability considerations unreliable.

720   **7. Conclusions**

In this study, we have systematically explored the impact of increasing obliquity on an Earth-like planet with a completely saturated lower boundary of small thermal inertia and no active ocean. Under these conditions, obliquity-induced insolation changes lead to significant changes in the atmospheric circulation.

725   These are dominated by changes in the solstitial Hadley circulation, which becomes increasingly broad and cross-equatorial as the insolation contrast between
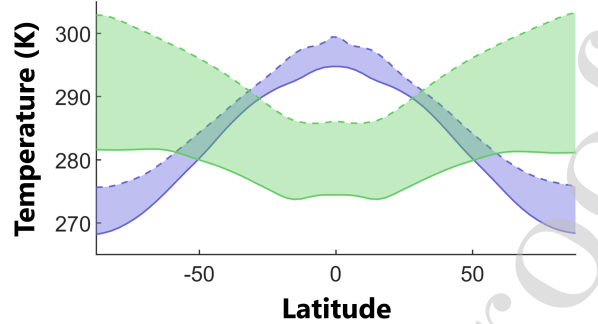
34

Figure 17: Annual-mean surface temperatures in $23.5°$(blue) and $85°$(green) obliquity simulations, with $\tau_{control}$. Results obtained with seasonally varying insolation are plotted with a solid line, while those resulting from annual-mean forcing are shown with a dashed line and the difference between the two is shaded.

the summer and winter hemispheres increases. The winter, cross-equatorial Hadley cell at high obliquity transports so much energy from the summer into the winter hemisphere as to significantly reduce the thermal contrast. The com-
730 bination of reduced temperature gradients in the winter extratropics and low temperatures (and hence moisture) leads, somewhat surprisingly, to a weakening of eddy activity and absence of precipitating storm tracks.

While becoming broader with increasing obliquity, the solstitial cross-equatorial Hadley cells do not become global even as temperature and MSE maximize at
735 the summer poles, in agreement with energetic and dynamical constraints on these circulations (e.g., Held & Hou, 1980; Lindzen & Hou, 1988; Guendelman & Kaspi, 2018; Hill et al., 2019). This is worth emphasizing, as in the Earth's literature, the maximum in lower-level MSE is commonly used as a proxy for the poleward extent of the zonally averaged and monsoonal Hadley circulations
740 (e.g., Privé & Plumb, 2007; Shekhar & Boos, 2016). It is clear that this constraint fails in a broader planetary context.

While not embedded within the ascending branch of the cross-equatorial Hadley cell, the summer poles in high-obliquity planets still experience non-negligible precipitation. This arises from both locally forced convection at the

35

745 peak of the summer, when the summer pole is the hottest place on the planet, and condensation of atmospheric water vapor at the end of the summer, as temperatures drop rapidly.

When considering habitability, the lower obliquity scenarios are at first glance more favorable candidates for life. These planets, such as our own, ex-
750 perience less extreme temperature variations throughout the year. Therefore, if the planet is in the habitable zone, it seems more likely that a large portion of the surface would be viable.

However, higher obliquities might not be as unfavorable to life as it might seem. Extreme temperature variations could be dampened, for example, by an
755 ocean, in which case the higher obliquity planets would be just as viable as the low obliquity cases. Even in the absence of an active ocean, the atmospheric circulation appears to be able to provide a pathway through which temperature extremes are significantly dampened. Caveats to bear in mind are the absence in our model of important feedbacks, such as those related to ice albedo and
760 clouds, which might have both quantitative and qualitative impacts on our results. These will be explored in future studies.

Furthermore, the response of the ITCZ and surface temperature gradients to obliquity leads to significant changes in the precipitation distribution at all latitudes. At high obliquities, the mid-to-high latitudes become regions of high
765 annual mean net precipitation, while the equator becomes a region of net evap- oration. Therefore, the distribution of wet and arid regions would be roughly reversed and this could alter which regions would most likely to be hospitable.

Thus, while we cannot make absolute statements about habitability and we have not sought to reproduce any individual planet, increased obliquity leads
770 to seasonal phenomena that shape in fundamental ways the planet's climate. Obliquity is therefore an important consideration for climate characterization, intensifying the need to not only study planetary mean climate but also seasonal behavior.

36

Acknowledgments

780 **References**

Adam, O., Bischoff, T., & Schneider, T. (2016). Seasonal and interannual variations of the energy flux equator and ITCZ. Part I: Zonally averaged ITCZ position. *Journal of Climate*, *29*, 3219–3230. doi:10.1175/JCLI-D-15-0512.1.

Barsugli, J. J., & Battisti, D. S. (1998). The basic effects of atmosphere-ocean
785   thermal coupling on midlatitude variability. *Journal of the Atmospheric Sciences*, *55*, 477–493. doi:10.1175/1520-0469(1998)055<0477:TBEOAO>2.0.CO;2.

Bischoff, T., & Schneider, T. (2014). Energetic Constraints on the Position of the Intertropical Convergence Zone. *Journal of Climate*, *27*, 4937–4951.
790   doi:10.1175/JCLI-D-13-00650.1.

Bordoni, S., & Schneider, T. (2008). Monsoons as eddy-mediated regime transitions of the tropical overturning circulation. *Nature Geosci*, *1*, 515–519. doi:10.1038/ngeo248.

Cronin, T. W., & Emanuel, K. A. (2013). The climate time scale in the approach
795   to radiative-convective equilibrium. *Journal of Advances in Modeling Earth Systems*, *5*, 843–849. doi:10.1002/jame.20049.

Del Genio, A., & Zhou, W. (1996). Simulations of Superrotation on Slowly Rotating Planets: Sensitivity to Rotation and Initial Condition. *Icarus*, *120*, 332–343. doi:10.1006/icar.1996.0054.

Emanuel, K. A., David Neelin, J., & Bretherton, C. S. (1994). On large-scale circulations in convecting atmospheres. *Quarterly Journal of the Royal Meteorological Society*, *120*, 1111–1143. doi:10.1002/qj.49712051902.

Faulk, S., Mitchell, J., Bordoni, S., Faulk, S., Mitchell, J., & Bordoni, S. (2017). Effects of rotation rate and seasonal forcing on the ITCZ extent in planetary atmospheres. *Journal of the Atmospheric Sciences*, (pp. JAS–D–16–0014.1). doi:10.1175/JAS-D-16-0014.1.

Ferreira, D., Marshall, J., O'Gorman, P. A., & Seager, S. (2014). Climate at high-obliquity. *Icarus*, *243*, 236–248. doi:10.1016/j.icarus.2014.09.015.

Frierson, D. M. W., & Hwang, Y. T. (2012). Extratropical influence on ITCZ shifts in slab ocean simulations of global warming. *Journal of Climate*, *25*, 720–733. doi:10.1175/JCLI-D-11-00116.1.

Frierson, D. M. W., Lu, J., & Chen, G. (2007). Width of the Hadley cell in simple and comprehensive general circulation models. *Geophysical Research Letters*, *34*. doi:10.1029/2007GL031115.

Gill, A. E. (1982). *Atmosphere-ocean dynamics*. Academic Press New York.

Guendelman, I., & Kaspi, Y. (2018). An Axisymmetric Limit for the Width of the Hadley Cell on Planets With Large Obliquity and Long Seasonality. *Geophysical Research Letters*, *45*, 13,213–13,221. doi:10.1029/2018GL080752.

Held, I. M., & Hou, A. Y. (1980). Nonlinear Axially Symmetric Circulations in a Nearly Inviscid Atmosphere. *Journal of the Atmospheric Sciences*, *37*, 515–533. doi:10.1175/1520-0469(1980)037<0515:NASCIA>2.0.CO;2.

Hill, S. A., Bordoni, S., & Mitchell, J. L. (2019). Axisymmetric constraints on cross-equatorial hadley cell extent. *Journal of the Atmospheric Sciences*, *76*, 1547–1564. doi:10.1175/JAS-D-18-0306.1.

Kang, S. M., Frierson, D. M. W., & Held, I. M. (2009). The Tropical Response to Extratropical Thermal Forcing in an Idealized GCM: The Importance of

Radiative Feedbacks and Convective Parameterization. *Journal of the Atmospheric Sciences*, *66*, 2812–2827. doi:10.1175/2009JAS2924.1.

Kang, S. M., Held, I. M., Frierson, D. M., & Zhao, M. (2008). The response of the
ITCZ to extratropical thermal forcing: Idealized slab-ocean experiments with a GCM. *Journal of Climate*, *21*, 3521–3532. doi:10.1175/2007JCLI2146.1.

Laskar, J., & Robutel, P. (1993). The chaotic obliquity of the planets. *Nature*, *361*, 608–612. doi:10.1038/361608a0.

Lindzen, R. S., & Hou, A. Y. (1988). Hadley circulations for zonally averaged heating centered off the equator. *Journal of the Atmospheric Sciences*, *45*, 2416–2427. doi:10.1175/1520-0469(1988)045<2416:HCFZAH>2.0.CO;2.

Lindzen, R. S., & Nigam, S. (1987). On the Role of Sea Surface Temperature Gradients in Forcing Low-Level Winds and Convergence in the Tropics. *Journal of the Atmospheric Sciences*, *44*, 2418–2436. doi:10.1175/1520-0469(1987)044<2418:OTROSS>2.0.CO;2.

Merlis, T. M., & Schneider, T. (2010). Atmospheric Dynamics of Earth-Like Tidally Locked Aquaplanets. *J. Adv. Model. Earth Syst.*, *2*, 1–17. doi:10.3894/JAMES.2010.2.13.

Merlis, T. M., Schneider, T., Bordoni, S., & Eisenman, I. (2013). The tropical precipitation response to orbital precession. *Journal of Climate*, *26*, 2010–2021. doi:10.1175/JCLI-D-12-00186.1.

Neelin, J. D., & Held, I. M. (1987). Modeling Tropical Convergence Based on the Moist Static Energy Budget. *Monthly Weather Review*, *115*, 3–12. doi:10.1175/1520-0493(1987)115<0003:MTCBOT>2.0.CO;2.

O'Gorman, P. A., & Schneider, T. (2008). The Hydrological Cycle over a Wide Range of Climates Simulated with an. *Journal of Climate*, *21*, 3815–3832. doi:10.1175/2007JCLI2065.1.

Pauluis, O. (2004). Boundary Layer Dynamics and Cross-Equatorial Hadley Circulation. *Journal of the Atmospheric Sciences*, *61*, 1161–1173. doi:10. 1175/1520-0469(2004)061<1161:BLDACH>2.0.CO;2.

Privé, N. C., & Plumb, R. A. (2007). Monsoon Dynamics with Interactive Forcing. Part I: Axisymmetric Studies. *Journal of the Atmospheric Sciences*, *64*, 1417–1430. doi:10.1175/JAS3916.1.

Schneider, T., & Bordoni, S. (2008). Eddy-Mediated Regime Transitions in the Seasonal Cycle of a Hadley Circulation and Implications for Monsoon Dynamics. *Journal of the Atmospheric Sciences*, *65*, 915–934. doi:10.1175/2007JAS2415.1.

Shekhar, R., & Boos, W. R. (2016). Improving energy-based estimates of monsoon location in the presence of proximal deserts. *Journal of Climate*, *29*, 4741–4761. doi:10.1175/JCLI-D-15-0747.1.

Showman, A. P., Wordsworth, R. D., Merlis, T. M., & Kaspi, Y. (2013). Atmospheric Circulation of Terrestrial Exoplanets. In *Comparative Climatology of Terrestrial Planets*. University of Arizona Press. doi:10.2458/azu_uapress_9780816530595-ch12.

Singh, M. S. (2019). Limits on the extent of the solsticial Hadley cell: the role of planetary rotation. *Journal of the Atmospheric Sciences*, (pp. 1989–2004). doi:10.1175/jas-d-18-0341.1.

Sobel, A. H., Bellon, G., & Bacmeister, J. (2007). Multiple equilibria in a single-column model of the tropical atmosphere. *Geophysical Research Letters*, *34*, 1–5. doi:10.1029/2007GL031320.

Sobel, A. H., & Bretherton, C. S. (2000). Modeling tropical precipitation in a single column. *Journal of Climate*, *13*, 4378–4392. doi:10.1175/1520-0442(2000)013<4378:MTPIAS>2.0.CO;2.

Touma, J., & Wisdom, J. (1993). The chaotic obliquity history of Mars. *Science*, *259*, 1294–1296. doi:10.1038/361608a0.

40

Turtle, E. P., Perry, J. E., McEwen, A. S., DelGenio, A. D., Barbara, J., West, R. A., Dawson, D. D., & Porco, C. C. (2009). Cassini imaging of Titan's high-latitude lakes, clouds, and south-polar surface changes. *Geophysical Research Letters*, *36*, n/a–n/a. doi:`10.1029/2008GL036186`.

885 Wang, H., & Richardson, M. I. (2015). The origin, evolution, and trajectory of large dust storms on Mars during Mars years 24–30 (1999–2011). *Icarus*, *251*, 112–127. doi:`10.1016/j.icarus.2013.10.033`.

Wei, H.-h., & Bordoni, S. (2018). Energetic constraints on the ITCZ in idealized simulations with a seasonal cycle. *Journal of Advances in Modeling Earth* 890 *Sciences (JAMES)*, (pp. 1–35).

Zhou, W., & Xie, S. P. (2018). A hierarchy of idealized monsoons in an intermediate GCM. *Journal of Climate*, *31*, 9021–9036. doi:`10.1175/JCLI-D-18-0084.1`.

41

MANUSCRIPT ICARUS_2018_458 "Atmosphere dynamics in high obliquity planets"

Ana H. Lobo and Simona Bordoni

Highlights:

- Increased obliquity leads to seasonal phenomena that shape the planet's climate.
- The Hadley cell in the solstice seasons becomes broader and more cross-equatorial, but not global.
- Winter eddy activity is weakened and precipitation storm tracks are absent.
- Moisture storage plays an important role for high-latitude rain at large obliquities.

Declaration of interests

☒ The authors declare that they have no known competing financial interests or personal relationships that could have appeared to influence the work reported in this paper.

☐The authors declare the following financial interests/personal relationships which may be considered as potential competing interests: